Journal of the European Ceramic Society 41 (2021) 2918–2922

Contents lists available at ScienceDirect

Journal of the European Ceramic Society

journal homepage: www.elsevier.com/locate/jeurceramsoc

Barium titanate-based bilayer functional coatings on Ti alloy biomedical implants

Kara K. Poon [a], Stefan Schafföner [a,b], Mari-Ann Einarsrud [a], Julia Glaum [a,*]

[a] Department of Materials Science and Engineering, NTNU Norwegian University of Science and Technology, Trondheim, Norway
[b] Department of Materials Science and Engineering and Institute of Materials Science, University of Connecticut, Storrs, CT, USA

ARTICLE INFO

Keywords:
Barium titanate
Ti6Al4V
Ceramic coating
Microstructure
EPMA WDS

ABSTRACT

Piezoelectric coatings have the ability to functionalise conventional structural materials into responsive devices. Today, piezoelectric coatings have been applied to both rigid and flexible substrates for sensing, actuating, and energy harvesting applications. We envision (Ba,Ca)(Zr,Ti)O_3 (BCZT) piezoelectric coatings for biomedical use such as *in vivo* sensing or electrical cell stimulation. However, reliable processing routes for the development of BCZT ceramics as a functionalisation coating on biomedical substrates are required. In this work, the synthesis of bilayer BCZT and $CaTiO_3$ ceramic coatings on Ti6Al4V metal substrates *via* spray-deposition and heat-treatment was investigated. For thin coatings, reactions at the metal/ceramic interface led to the development of a porous interface reaction region partly consisting of CaO. The hygroscopicity of CaO affects the adhesion of the coating to Ti6Al4V at ambient conditions. Minimisation of the kinetic contributions to these interface reactions were achieved by increasing the coating thickness.

1. Introduction

Piezoelectric ceramics are utilised in many applications including sensing, actuation, and energy harvesting due to their electromechanical characteristics. For novel electronic devices, such as random access memories, structural health monitoring, and microelectromechanical systems, the development of ceramic coatings on metal substrates is essential to allow integration with existing device platforms [1–3].

In these applications, piezoelectric ceramic coatings have primarily been developed from Pb(Zr,Ti)O_3 (PZT) due to the exceptionally high piezoelectric response, and have been deposited onto substrates including steel, copper, and nickel [4–7].

A novel application for piezoelectric materials is in the biomedical field, especially for *in vivo* sensing and electrical cell stimulation for provoking specific cell responses [8–10]. For the translation of piezoelectric coatings to this field, lead-free materials are necessary to avoid lead poisoning. Furthermore, the ceramic material should be integrable on metal substrate materials commonly used in the desired application. One promising candidate for the implementation in biomedical devices is barium titanate (BT). Development of BT-based ceramic coatings have been reported for Ti6Al4V substrates, a Ti-alloy that is primarily used for hard tissue replacement such as in dental or joint implants using plasma electrolytic oxidation, as well as for TiNb substrates using pulsed laser deposition [11,12]. In addition, current biomedical ceramic coatings such as hydroxyapatite are often deposited on Ti6Al4V [13]. This is due to the combination of high Young's modulus, fracture toughness, corrosion resistance, and strength to weight ratio values that are more suited to load-bearing applications than the values for ceramics including BT-based materials [14–19].

We envisage (Ba,Ca)(Zr,Ti)O_3 (BCZT) piezoelectric ceramics as functional coatings on Ti6Al4V for *in vivo* cell stimulation directly at an implant site. BCZT has been shown to be non-cytotoxic and to exhibit an exceptional piezoelectric response higher than BT ceramics [20–24]. In this study, we investigate a spray-deposition and heat-treatment process for the development of BCZT coatings on Ti6Al4V substrates with a $CaTiO_3$ interlayer. $CaTiO_3$ has been shown to improve the bioactivity of Ti6Al4V dental implants [25] and was chosen due to its thermal expansion coefficient bridging the characteristics of Ti6Al4V and BCZT. Spray-deposition was selected for its versatility, cost efficiency, and application relevance. Although it is a line-of-sight technique, the mobility of the nozzle or substrate during spray-coating allows for the deposition of coatings on curved substrates. During heat-treatment,

* Corresponding author at: Department of Materials Science and Engineering, NTNU Norwegian University of Science and Technology, Sem Sælands vei 12, 7491 Trondheim, Norway.
E-mail addresses: julia.glaum@ntnu.no, j.glaum@posteo.net (J. Glaum).

https://doi.org/10.1016/j.jeurceramsoc.2020.12.023
Received 4 September 2020; Received in revised form 8 December 2020; Accepted 11 December 2020
Available online 17 December 2020

interface reactions caused the formation of a porous interface reaction region between Ti6Al4V and $CaTiO_3$ for thin bilayer ceramic coatings. Hygroscopic CaO was formed and significantly impaired the adhesive quality of the ceramic coatings to the metal substrate over time. Increasing the thickness of the ceramic layers kinetically hindered these interface reactions and the microstructure of the coatings remained stable.

2. Materials and methods

2.1. Ceramic coating synthesis

Ceramic coatings on Ti6Al4V were formed from calcined $(Ba_{0.9}Ca_{0.1})(Zr_{0.1}Ti_{0.9})O_3$ and as-received $CaTiO_3$ ceramic powders (≥ 99 %, Sigma Aldrich). Based on the BCZT phase diagram, the $(Ba_{0.9}Ca_{0.1})(Zr_{0.1}Ti_{0.9})O_3$ composition was chosen for its tendency to display good and stable piezoelectric properties under mechanical loading conditions, relevant for the potential application as a load-bearing implant material [26]. $CaTiO_3$ was chosen as a suitable interlayer to reduce the thermal expansion coefficient mismatch between Ti6Al4V and BCZT ($TEC_{Ti6Al4V} = 10.3 \times 10^{-6}$ K^{-1} (600–1000 °C) [27], $TEC_{CaTiO_3} = 12.2 \times 10^{-6}$ K^{-1} (30–700 °C) [28], $TEC_{BT} = 17.5 \times 10^{-6}$ K^{-1} (350–1050 °C) [29]). BCZT ceramic powders were synthesised following the solid-state approach, as described in reference [22]. $BaCO_3$ (≥ 99.98 %, Sigma Aldrich), $CaCO_3$ (≥ 99 %, Sigma Aldrich), ZrO_2 (≥ 99.978 %, Alfa Aesar), and TiO_2 (≥ 99.8 %, Sigma Aldrich) were selected as precursor materials. Pellets calcined at 1300 °C for 2 h were ground using an agate mortar and pestle, sieved with a 250 µm mesh, wet ball-milled with 96 % ethanol and 5 mm diameter yttria-stabilised zirconia milling balls for 24 h on a long roll jar mill, and dried using a rotary evaporator. The dried calcined powders were thereafter sieved through a 250 µm mesh. The particle size of the calcined BCZT and as-received $CaTiO_3$ powders were ≈ 0.76 ± 0.20 µm and ≈ 0.41 ± 0.09 µm, respectively, as determined following the linear intercept method on at least 50 intersections from SEM micrographs.

Ceramic slurries were prepared by ultra-sonicating suspensions of ceramic powders in 96 % ethanol (0.05 g/mL, Ultrasonic Needle, Branson Ultrasonics Corp., USA). In preparation for deposition, Ti6Al4V (Grade 5, ASTM B265 [30]) metal substrates (10 × 10 × 1 mm^3, ANKURO Int. GmbH, Germany) were grinded with #1200 SiC paper, degreased with detergent and ethanol, dried using lint-free paper, and pre-heated to 100 °C.

Coatings were deposited in layers within 1 h of substrate preparation using an Aztek spray-coating gun (0.7 µm nozzle size, 0.5 bar pressurised air, Testors, USA). After each ceramic slurry layer (1−5 µm in thickness) was deposited, samples were transferred to a heating cabinet at 100 °C for 20 s before a subsequent layer was deposited.

Heat-treatment was performed in zirconia crucibles in a tube furnace (Entech Horizontal Tube Furnace, Entech Energiteknik, Sweden) at 900 °C for 1 h under Ar atmosphere (0.6 Nl/min), with heating and cooling rates of 200 °C/h. Prior to heat-treatment, the tube furnace was evacuated to 0.6–0.8 mbar and purged at least three times with Ar gas (Argon 5.0, ≥ 99.999 % purity).

The samples were stored in a desiccator at 23 °C and a relative humidity of 23 %.

2.2. Imaging, elemental and phase analyses

Micrographs were obtained using scanning electron microscopy (SEM) (Ultra 55, Carl Zeiss AG, Germany). In preparation for SEM imaging, entire ceramic-coated metal substrates were cold-mounted in epoxy (EpoFix Resin & Hardener, Struers Inc., USA). To expose the metal/ceramic cross-section, the 1 mm side of a sample was grinded to a depth of at least 3 mm into the sample and to a surface finish of 0.25 µm, and the surface was coated with carbon for imaging. Element distributions across the metal/ceramic interface were determined using electron probe microanalysis wavelength dispersive spectroscopy (EPMA WDS) (JEOL JXA-8500 F, JEOL Ltd., Japan). The phase compositions at the metal/ceramic interface were determined by X-ray diffraction (XRD) measurements (D8 A25 DaVinci X-ray Diffractometer, Bruker, USA) using Cu Kα radiation of 1.54 Å.

3. Results

3.1. Samples with coating thickness < 80 µm

For ceramic coatings of < 80 µm in thickness, a porous interface reaction region of ≈ 2 µm in thickness tended to form at the interface between Ti6Al4V and $CaTiO_3$ upon heat treatment, as shown in Fig. 1 (a). In addition, two microstructurally distinct $CaTiO_3$ regions were apparent. The region adjacent to the Ti6Al4V substrate, labelled as $CaTiO_3(1)$, appeared to be denser, while the region adjacent to the BCZT coating, denoted as $CaTiO_3(2)$, was coarser. When observed from the top view, the ceramic coating was well-attached and homogeneous (Fig. 1 (b)). However, after storing for several weeks at constant temperature and relative humidity (23 °C and 23 %), crack formation through the $CaTiO_3$ coating was observed (Fig. 1 (c)), as well as pronounced peeling and delamination (Fig. 1 (d)).

WDS line scans were performed to determine the element distributions through the metal/ceramic cross-sections containing the porous interface reaction region, as shown in Fig. 2. Oxygen was detected at the porous interface reaction region, $CaTiO_3$ and BCZT coatings, with increasing concentration towards the surface of the coated substrate. The porous interface reaction region also contained Ca, but in lower concentration than the bulk $CaTiO_3$ coating. With respect to the two microstructurally distinct $CaTiO_3$ regions, $CaTiO_3(1)$ is Ca-deficient compared to $CaTiO_3(2)$. Diffusion of Al and V was observed from the Ti6Al4V substrate into the porous interface reaction region, but not beyond into the $CaTiO_3$ coating. The concentration of Ti remained stable through the Ti6Al4V substrate and decreased within the porous interface reaction region towards the surface of the coated substrate. Some interdiffusion of Ca and Ba was observed at the $CaTiO_3$/BCZT interface. Values at the crack region are not discussed because the topographical feature alters X-ray scattering behaviour, which therefore significantly affects the results. Similarly, only qualitative analyses of the trends in

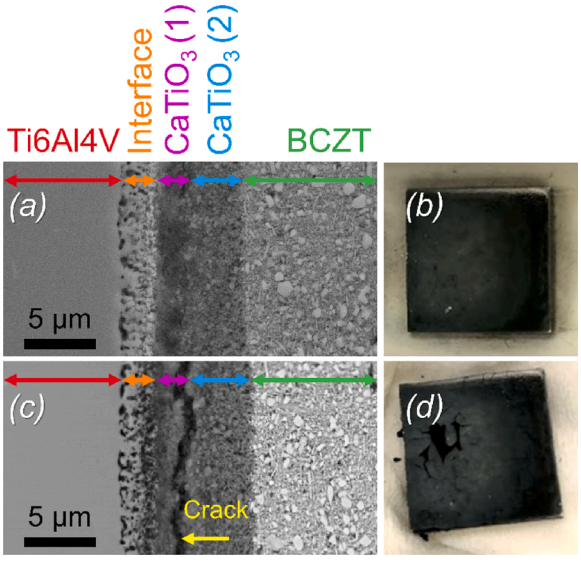

Fig. 1. SEM cross-sectional micrographs and photographs of $CaTiO_3$- and BCZT-coated Ti6Al4V (a, b) immediately after synthesis and (c, d) after storing for several weeks in an environment with constant temperature and relative humidity (23 °C and 23 %). Crack formation, peeling, and delamination were observed after storage.

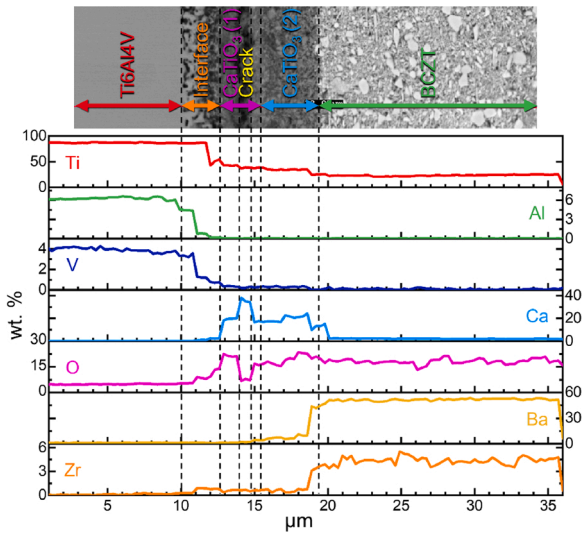

Fig. 2. EPMA WDS line scans of $CaTiO_3$- and BCZT-coated Ti6Al4V containing the porous interface reaction region. The line scans display the element distributions of Ti, Al, V, Ca, O, Ba, and Zr across the metal/ceramic interface.

the element distributions across the interface were performed as the porous interface reaction region, $CaTiO_3$ and BCZT coatings are not fully dense.

An XRD pattern of a $CaTiO_3$- and BCZT-coated sample that displayed coating delamination after storage is presented in Fig. 3. At the delaminated interface, BCZT and $CaTiO_3$ were detected, as expected, as well as $TiO_{0.84}$ and $Ca(OH)_2$ (PDF cards 04-020-5213, 00-022-0153, 04-006-1902, and 01-070-5492, respectively [31]).

3.2. Samples with coating thickness > 80 μm

Fig. 4 shows a representative SEM micrograph of the metal/ceramic cross-section for ceramic coatings > 80 μm in thickness. In contrast to the thinner coatings (Fig. 1), no reaction regions at the metal-ceramic interface appeared. Instead, clear distinctions between the three materials, Ti6Al4V, $CaTiO_3$, and BCZT, were observed. Slight delamination between Ti6Al4V and $CaTiO_3$ can be seen, as highlighted by the magnified region in Fig. 4, but both layers of $CaTiO_3$ and BCZT appeared well-attached and well-packed.

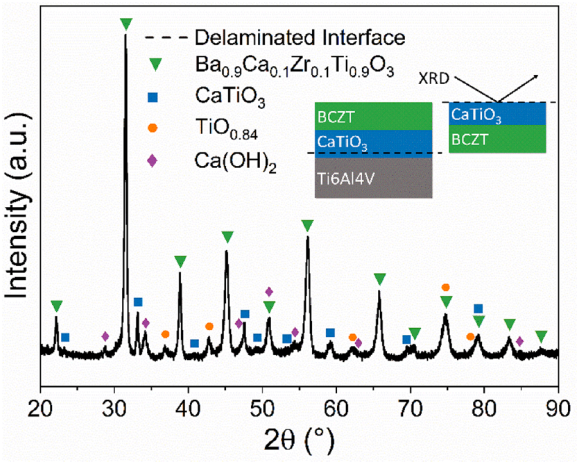

Fig. 3. XRD diffractogram of the delaminated metal/ceramic interface of $CaTiO_3$- and BCZT-coated Ti6Al4V (as described in the inset figure schematic). The diffractogram is matched with PDF 04-020-5213 $Ba_{0.9}Ca_{0.1}Zr_{0.1}Ti_{0.9}O_3$, PDF 00-022-0153 $CaTiO_3$, PDF 04-006-1902 $TiO_{0.84}$, and PDF 01-070-5492 $Ca(OH)_2$.

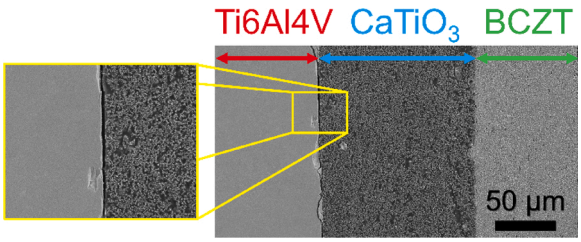

Fig. 4. SEM micrograph of $CaTiO_3$- and BCZT-coated Ti6Al4V with a total ceramic coating thickness of ≈ 200 μm.

4. Discussion

The mechanism of the porous interface reaction region formation

Based on the element distributions and phase analysis of the porous interface reaction region, it is proposed that several interface reactions occur during heat-treatment giving rise to the porous interface reaction region and the differing $CaTiO_3$ microstructures for ceramic coatings of < 80 μm in thickness. An illustration of the metal/ceramic cross-section and a brief description of the interface reactions are displayed in Fig. 5.

The porous interface reaction region arises from partial oxidation of the Ti6Al4V substrate, as described by:

$$Ti(s) + \frac{x}{2}O_2\ (g) \rightarrow TiO_x(s) \quad (1)$$

$$2Al(s) + \frac{3}{2}O_2(g) \rightarrow Al_2O_3(s) \quad (2)$$

$$V(s) + \frac{x}{2}O_2(g) \rightarrow VO_x(s) \quad (3)$$

where oxygen arises from two sources. The first source is oxygen in the inert Ar gas during heat-treatment in the tube furnace. It is expected that a constant oxygen partial pressure of 0.2 Pa is maintained, as calculated using the oxygen partial pressure of the Ar gas, the ideal gas law, Dalton's law, and a furnace volume of $1.13 \cdot 10^{-3}$ m^3.

The second source of oxygen is from the reduction of Ti^{4+} in $CaTiO_3$ due to the low oxygen partial pressure in the furnace and at the interface to the Ti6Al4V substrate, as follows:

$$CaTiO_3(s) \rightarrow CaTiO_{3-\delta}(s) + \frac{\delta}{2}O_2(g) \quad (4)$$

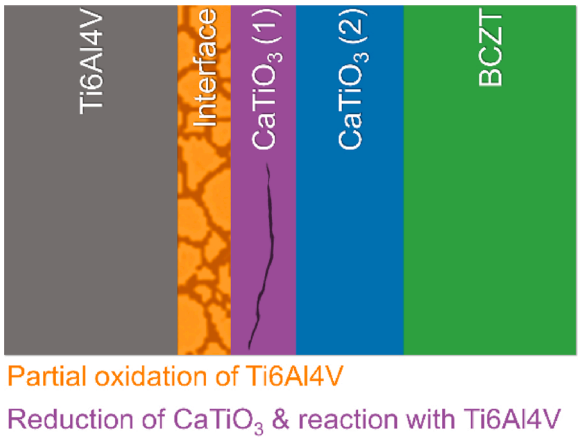

Fig. 5. Illustration of the metal/ceramic cross-section. The porous interface reaction region (orange) arises from oxidation of the Ti6Al4V substrate. The two microstructurally distinct $CaTiO_3$ regions (purple & blue) are apparent due to the reduction of $CaTiO_3$ when in contact with Ti6Al4V. (For interpretation of the references to colour in this figure legend, the reader is referred to the web version of this article).

Eqs. (1–3) are corroborated by the detection of Ti, Al, V, and O at the porous interface reaction region in the WDS line scans (Fig. 2). Additionally, Eq. (1) is confirmed by the detection of $TiO_{0.84}$ from XRD analyses at the delaminated coating interface (Fig. 3). The enrichment of Al at the porous interface reaction region has similarly been observed during cyclic oxidation of Ti6Al4V [32]. Moreover, the partial oxidation of Ti6Al4V is confirmed by the porous appearance of the interface reaction region shown in Fig. 1 (a). The microstructure is reminiscent of the Kirkendall effect, describing the creation of voids due to dissimilar atom diffusion rates across an interface [33]. Similar microstructures have been observed between metal/metal and metal/oxide interfaces [34,35].

In contact with Ti of the Ti6Al4V substrate, $CaTiO_{3-\delta}$ from Eq. (4) can be further reduced to form $TiO_{1-\delta 2}$ and CaO as reaction products:

$$Ti(s) + CaTiO_{3-\delta}(s) \rightarrow 2TiO_{1-\delta 2}(s) + CaO(s) \quad (5)$$

The estimated equilibrium oxygen partial pressure at the Ti6Al4V/$CaTiO_{3-\delta}$ interface is $5.3 \cdot 10^{-40}$ Pa [36] assuming an oxygen content of 0.2 wt% (0.57 mol%) in Ti6Al4V [30] and a temperature of 900 °C. Due to the low oxygen partial pressure at the Ti6Al4V/$CaTiO_{3-\delta}$ interface, Ti in the reaction product $TiO_{1-\delta 2}$ will not stabilise as Ti^{4+} nor Ti^{3+}, but rather at a lower oxidation state or as a solid solution [37]. This is observed by the detection of $TiO_{0.84}$ at the delaminated coating interface from XRD analyses (Fig. 3). Critically, the formation of CaO, a highly hygroscopic compound [38], degrades the structural integrity of the ceramic coating in ambient conditions [39]. Upon reaction with moisture in the air, CaO forms $Ca(OH)_2$ and expands, causing crack evolution during storage. The presence of $Ca(OH)_2$ at the metal/ceramic interface was confirmed in the XRD pattern (Fig. 3).

The presence of Ca in the porous interface reaction region, as shown in the WDS line scans (Fig. 2), indicates a time-dependent effect during heat-treatment. The partial oxidation of Ti6Al4V creates the porous interface reaction region, which is initially thin enough to allow the reduction reaction in Eq. (5) to proceed. However, at a threshold thickness, the porous interface reaction region becomes thick enough to act as a separation layer between Ti6Al4V and $CaTiO_{3-\delta}$, limiting further reduction. This enables the reverse reaction to occur, where CaO reacts with $TiO_{1-\delta 2}$ to form the more stable $CaTiO_{3-\delta}$ at the porous interface reaction region.

The microstructural distinction between the $CaTiO_3$ regions, $CaTiO_3$(1) and $CaTiO_3$(2) (Fig. 1 (a)), arises from the different stoichiometries induced by the reduction reactions described above. The $CaTiO_3$(2) region is less affected by the reduction reactions described by Eqs. (4) and (5) as it is distant from Ti6Al4V and not in contact with the reducing medium, Ti. In contrast, $CaTiO_3$(1), which is adjacent to the Ti6Al4V substrate is more strongly affected by reduction and by diffusion across the Ti6Al4V/$CaTiO_3$ interface. This results in a $CaTiO_3$(2) region that is less oxygen deficient than the $CaTiO_3$(1) region (*i.e.* δ in the $CaTiO_3$(2) region is smaller than in the $CaTiO_3$(1) region), influencing the diffusion processes that occur during sintering and subsequently, the densification and grain growth behaviour of the two $CaTiO_3$ regions.

The oxygen content within the $CaTiO_3$ layer is calculated to be $2.5–5.7 \cdot 10^{-4}$ mol for a powder mass of 0.06–0.13 g, suggesting that it should be the primary source of oxygen. However, the different microstructures observed for thin (< 80 μm) and thick (> 80 μm) bilayer ceramic coatings highlight that the ceramic coating thickness strongly influences diffusion processes and sintering behaviour. The tendency for the porous interface reaction region and two microstructurally distinct $CaTiO_3$ regions to be formed for ceramic coating thicknesses of < 80 μm (Fig. 1) show that the interface reactions are kinetically driven by the diffusion of oxygen gas from the Ar environment through the porous structure of the ceramic coatings to the Ti6Al4V substrate. In contrast, ceramic coatings of > 80 μm in thickness did not tend to form the porous interface reaction region and showed only one microstructurally distinct $CaTiO_3$ region (Fig. 4). The larger thickness of the coatings kinetically hindered the diffusion of oxygen gas to the Ti6Al4V substrate, suppressing the reactions described by Eqs. (1–3). The tendency for the porous interface reaction region formation is therefore likely dominated by the diffusion of higher mobility oxygen gas through the ceramic coatings compared to lower mobility O^{2-} in the $CaTiO_3$ lattice in the interlayer.

5. Conclusions

In this work, BCZT ceramic coatings were spray-deposited onto Ti6Al4V with a $CaTiO_3$ interlayer and heat-treated at 900 °C for 1 h under Ar atmosphere. During heat-treatment, a porous interface reaction region formed between Ti6Al4V and $CaTiO_3$. Crack formation was observed after storing samples at constant temperature and relative humidity for several weeks. This behaviour is attributed to interface reactions between Ti6Al4V and $CaTiO_3$ and the subsequent formation of highly hygroscopic CaO. To minimise the interface reactions, it is recommended that the ceramic coating be tailored to > 80 μm in thickness to kinetically hinder diffusion of oxygen in the Ar gaseous environment to the Ti6Al4V/$CaTiO_3$ interface. Alternatively, the Ti6Al4V substrate could be pre-oxidised prior to deposition of the ceramic slurries. An oxidised Ti6Al4V surface layer can act as a separation barrier [40], preventing the reaction between Ti6Al4V and $CaTiO_3$ and the subsequent formation of the detrimental CaO compound during heat-treatment. However, it is pertinent to limit pre-oxidation treatments to low temperatures, as oxidation of Ti6Al4V at temperatures exceeding 800 °C can cause the formation of a weakly adhered oxide layer prone to spalling [41].

Funding

The authors acknowledge funding provided by The Research Council of Norway [FRINATEK Project No. 250098] and by Horizon 2020 Marie Skłodowska-Curie Actions [H2020 MSCA 655866].

CRediT authorship contribution statement

Kara K. Poon: Conceptualization, Data curation, Formal analysis, Investigation, Methodology, Validation, Visualization, Writing - original draft. **Stefan Schafföner:** Formal analysis, Writing - review & editing. **Mari-Ann Einarsrud:** Formal analysis, Writing - review & editing, Supervision. **Julia Glaum:** Conceptualization, Funding acquisition, Methodology, Project administration, Supervision, Writing - review & editing.

Declaration of Competing Interest

The authors report no declarations of interest.

Acknowledgements

The authors gratefully acknowledge Morten Peder Raanes (senior engineer, Department of Materials Science and Engineering, NTNU) for his assistance in performing the EPMA WDS experiments.

Appendix A. Supplementary data

Supplementary material related to this article can be found, in the online version, at doi:https://doi.org/10.1016/j.jeurceramsoc.2020.12.023.

References

[1] N. Izyumskaya, Y.I. Alivov, S.J. Cho, H. Morkoç, H. Lee, Y.S. Kang, Processing, structure, properties, and applications of PZT thin films, Crit. Rev. Solid State Mater. Sci. 32 (2007) 111–202, https://doi.org/10.1080/10408430701707347.

[2] S. Chen, C.K.I. Tan, S.Y. Tan, S. Guo, L. Zhang, K. Yao, Potassium sodium niobate (KNN)-based lead-free piezoelectric ceramic coatings on steel structure by thermal spray method, J. Am. Ceram. Soc. 101 (2018) 5524–5533, https://doi.org/10.1111/jace.15820.

[3] Y. Tsujiura, E. Suwa, F. Kurokawa, H. Hida, K. Suenaga, K. Shibata, I. Kanno, Lead-free piezoelectric MEMS energy harvesters of (K,Na)NbO_3 thin films on stainless steel cantilevers, Jpn. J. Appl. Phys. 52 (2013), https://doi.org/10.7567/JJAP.52.09KD13, 09KD13.

[4] T. Suzuki, I. Kanno, J.J. Loverich, H. Kotera, K. Wasa, Characterization of Pb(Zr,Ti)O_3 thin films deposited on stainless steel substrates by RF-magnetron sputtering for MEMS applications, Sens. Actuators, A 125 (2006) 382–386, https://doi.org/10.1016/j.sna.2005.08.010.

[5] T. Fujii, Y. Hishinuma, T. Mita, T. Naono, Characterization of Nb-doped Pb(Zr,Ti)O_3 films deposited on stainless steel and silicon substrates by RF-magnetron sputtering for MEMS applications, Sens. Actuators, A 163 (2010) 220–225, https://doi.org/10.1016/j.sna.2010.08.019.

[6] A.I. Kingon, S. Srinivasan, Lead zirconate titanate thin films directly on copper electrodes for ferroelectric, dielectric and piezoelectric applications, Nat. Mater. 4 (2005) 233–237, https://doi.org/10.1038/nmat1334.

[7] R. Gupta, M. Tomar, V. Gupta, Y. Zhou, A. Chopra, S. Priya, A.S. Bhalla, R. Guo, Giant magnetoelectric effect in PZT thin film deposited on nickel, Energy Harvest. Syst. 3 (2016) 181–188, https://doi.org/10.1515/ehs-2015-0010.

[8] P. Mehrotra, Biosensors and their applications – a review, J. Oral Biol. Craniofacial Res. 6 (2016) 153–159, https://doi.org/10.1016/j.jobcr.2015.12.002.

[9] A. Marino, G.G. Genchi, E. Sinibaldi, G. Ciofani, Piezoelectric effects of materials on bio-interfaces, Appl. Mater. Interfaces 9 (2017) 17663–17680, https://doi.org/10.1021/acsami.7b04323.

[10] A.H. Rajabi, M. Jaffe, T.L. Arinzeh, Piezoelectric materials for tissue regeneration: a review, Acta Biomater. 24 (2015) 12–23, https://doi.org/10.1016/j.actbio.2015.07.010.

[11] Y. Mao, J. Yan, L. Wang, W. Dong, Y. Jia, X. Hu, X. Wang, Formation and properties of bioactive barium titanate coatings produced by plasma electrolytic oxidation, Ceram. Int. 44 (2018) 12978–12986, https://doi.org/10.1016/J.CERAMINT.2018.04.115.

[12] M. Jelínek, P. Vaněk, Z. Tolde, E. Buixaderas, T. Kocourek, V. Studnička, J. Drahokoupil, J. Petzelt, J. Remsa, M. Tyunina, PLD prepared bioactive $BaTiO_3$ films on TiNb implants, Mater. Sci. Eng. C 70 (2017) 334–339, https://doi.org/10.1016/J.MSEC.2016.08.072.

[13] M. Saini, Y. Singh, P. Arora, V. Arora, K. Jain, Implant biomaterials: a comprehensive review, World J. Clin. Cases 3 (2015) 52–57, https://doi.org/10.12998/wjcc.v3.i1.52.

[14] AZoM, Titanium Alloys - Ti6Al4V Grade 5, AZoM - Titan. Inf. Gr., 2002. http://www.azom.com/properties.aspx?ArticleID=1547.

[15] M. Geetha, A.K. Singh, R. Asokamani, A.K. Gogia, Ti based biomaterials, the ultimate choice for orthopaedic implants – a review, Prog. Mater. Sci. 54 (2009) 397–425, https://doi.org/10.1016/j.pmatsci.2008.06.004.

[16] A. Butscher, M. Bohner, S. Hofmann, L. Gauckler, R. Müller, Structural and material approaches to bone tissue engineering in powder-based three-dimensional printing, Acta Biomater. 7 (2011) 907–920, https://doi.org/10.1016/j.actbio.2010.09.039.

[17] A. Srinivas, R.V. Krishnaiah, V.L. Niranjani, S.V. Kamat, T. Karthik, S. Asthana, Ferroelectric, piezoelectric and mechanical properties in lead free (0.5)Ba($Zr_{0.2}Ti_{0.8}$)O_3–(0.5)($Ba_{0.7}Ca_{0.3}$)TiO_3 electroceramics, Ceram. Int. 41 (2015) 1980–1985, https://doi.org/10.1016/j.ceramint.2014.08.127.

[18] M. Vögler, M. Acosta, D.R.J. Brandt, L. Molina-Luna, K.G. Webber, Temperature-dependent R-curve behavior of the lead-free ferroelectric 0.615Ba($Zr_{0.2}Ti_{0.8}$)O_3-0.385($Ba_{0.7}Ca_{0.3}$)TiO_3 ceramic, Eng. Fract. Mech. 144 (2015) 68–77, https://doi.org/10.1016/j.engfracmech.2015.06.069.

[19] P. Sailaja, N. Pavan Kumar, N. Shara Sowmya, A.R. James, A. Kumar, R. Arockiakumar, A. Srinivas, Investigation of ferroelectric, piezoelectric and mechanically coupled properties of lead-free ($Ba_{0.85}Ca_{0.15}$)($Zr_{0.1}Ti_{0.9}$)O_3 ceramics, Adv. Appl. Ceram. 118 (2019) 300–307, https://doi.org/10.1080/17436753.2019.1573565.

[20] N.D. Scarisoreanu, F. Craciun, V. Ion, R. Birjega, A. Bercea, V. Dinca, M. Dinescu, L. E. Sima, M. Icriverzi, A. Roseanu, L. Gruionu, G. Gruionu, Lead-free piezoelectric (Ba,Ca)(Zr,Ti)O_3 thin films for biocompatible and flexible devices, ACS Appl. Mater. Interfaces 9 (2017) 266–278, https://doi.org/10.1021/acsami.6b14774.

[21] W. Liu, X. Ren, Large piezoelectric effect in Pb-free ceramics, Phys. Rev. Lett. 103 (2009) 1–4, https://doi.org/10.1103/PhysRevLett.103.257602.

[22] K.K. Poon, M.C. Wurm, D.M. Evans, M.A. Einarsrud, R. Lutz, J. Glaum, Biocompatibility of (Ba,Ca)(Zr,Ti)O_3 piezoelectric ceramics for bone replacement materials, J. Biomed. Mater. Res. - Part B Appl. Biomater. 108 (2020) 1295–1303, https://doi.org/10.1002/jbm.b.34477.

[23] B. Jaffe, W.R. Cook, H. Jaffe, Piezoelectric Ceramics, Academic Press, London, 1971.

[24] Y. Tan, J. Zhang, Y. Wu, C. Wang, V. Koval, B. Shi, H. Ye, R. McKinnon, G. Viola, H. Yan, Unfolding grain size effects in barium titanate ferroelectric ceramics, Sci. Rep. 5 (2015) 1–9, https://doi.org/10.1038/srep09953.

[25] H. Katsui, T. Goto, Bio-ceramic coating of Ca–Ti–O system compound by laser chemical vapor deposition. Interface Oral Heal. Sci. 2016, Springer Singapore, Singapore, 2017, pp. 47–62, https://doi.org/10.1007/978-981-10-1560-1_4.

[26] M.C. Ehmke, J. Daniels, J. Glaum, M. Hoffman, J.E. Blendell, K.J. Bowman, Reduction of the piezoelectric performance in lead-free (1-x)Ba($Zr_{0.2}Ti_{0.8}$)O_3-x($Ba_{0.7}Ca_{0.3}$)TiO_3 piezoceramics under uniaxial compressive stress, J. Appl. Phys. 112 (2012) 0–5, https://doi.org/10.1063/1.4768273.

[27] M. Wei, A.J. Ruys, B.K. Milthorpe, C.C. Sorrell, J.H. Evans, Electrophoretic deposition of hydroxyapatite coatings on metal substrates: a nanoparticulate dual-coating approach, J. Sol-Gel Sci. Technol. 21 (2001) 39–48, https://doi.org/10.1023/A:1011201414651.

[28] Y. Jiang, R. Guo, A.S. Bhalla, Growth and properties of $CaTiO_3$ single crystal fibers, J. Electroceram. 2 (1998) 199–203, https://doi.org/10.1023/A:1009978901009.

[29] J.A. Bland, The thermal expansion of cubic barium titanate ($BaTiO_3$) from 350 °C to 1050 °C, Can. J. Phys. 37 (1959) 417–421, https://doi.org/10.1139/p59-046.

[30] ASTM International, B265-20a: Standard Specification for Titanium and Titanium Alloy Strip, Sheet, and Plate, 2020, https://doi.org/10.1520/B0265-20A.

[31] International Center for Diffraction Data, (2016).

[32] S. Zeng, A. Zhao, H. Jiang, X. Fan, X. Duan, X. Yan, Cyclic oxidation behavior of the Ti-6Al-4V alloy, Oxid. Met. 81 (2014) 467–476, https://doi.org/10.1007/s11085-013-9458-z.

[33] H.J. Fan, U. Gösele, M. Zacharias, Formation of nanotubes and hollow nanoparticles based on Kirkendall and diffusion processes: a review, Small 3 (2007) 1660–1671, https://doi.org/10.1002/smll.200700382.

[34] D. Mo, T. Song, Y. Fang, X. Jiang, C.Q. Luo, M.D. Simpson, Z. Luo, A review on diffusion bonding between titanium alloys and stainless steels, Adv. Mater. Sci. Eng. (2018) 15.

[35] A.-A. El Mel, R. Nakamura, C. Bittencourt, The Kirkendall effect and nanoscience: hollow nanospheres and nanotubes, Beilstein J. Nanotechnol. 6 (2015) 1348–1361, https://doi.org/10.3762/bjnano.6.139.

[36] M. Cancarevic, M. Zinkevich, F. Aldinger, Thermodynamic description of the Ti-O system using the associate model for the liquid phase, Calphad Comput. Coupling Phase Diagrams Thermochem. 31 (2007) 330–342, https://doi.org/10.1016/j.calphad.2007.01.009.

[37] M. Serratos, A. Bronson, The effect of oxygen partial pressure on the stability of Magneli phases in high temperature corrosive wear, Wear 198 (1996) 267–270, https://doi.org/10.1016/0043-1648(96)06986-4.

[38] Calcium oxide, CID=14778, Natl. Cent. Biotechnol. Information. PubChem Database. (n.d.). https://pubchem.ncbi.nlm.nih.gov/compound/Calcium-oxide.

[39] S. Schafföner, M. Bach, C. Jahn, L. Freitag, C.G. Aneziris, Advanced refractories for titanium metallurgy based on calcium zirconate with improved thermomechanical properties, J. Eur. Ceram. Soc. 39 (2019) 4394–4403, https://doi.org/10.1016/j.jeurceramsoc.2019.06.007.

[40] J. Dai, J. Zhu, C. Chen, F. Weng, High temperature oxidation behavior and research status of modifications on improving high temperature oxidation resistance of titanium alloys and titanium aluminides: a review, J. Alloys Compd. 685 (2016) 784–798, https://doi.org/10.1016/j.jallcom.2016.06.212.

[41] S. Kumar, T.S.N. Sankara Narayanan, S. Ganesh Sundara Raman, S.K. Seshadri, Thermal oxidation of Ti6Al4V alloy: microstructural and electrochemical characterization, Mater. Chem. Phys. 119 (2010) 337–346, https://doi.org/10.1016/j.matchemphys.2009.09.007.